Electrochemical oxygen generator with 99.9% oxygen purity and high energy efficiency

Yu Zhang
University of Science and Technology of China
Ke Xie
Fuzhou University
Fangyao Zhou
University of Science and Technology of China
Feiteng Wang
Nanjing University
Qian Xu
University of Science and Technology of China
Jun Hu
University of Science and Technology of China
Honghe Ding
University of Science and Technology of China
Peng Li
University of Science and Technology of China
Yi Tan
University of Science and Technology of China
Deming Li
University of Science and Technology of China
Junfa Zhu
University of Science and Technology of China
Changming Zhao (zhaocm@mail.ustc.edu.cn)
University of Science and Technology of China
Sen Lin (slin@fzu.edu.cn)
Fuzhou University
Yuen Wu (yuenwu@ustc.edu.cn)
University of Science and Technology of China

Research Article

Keywords: Oxygen generator, Electrochemical oxygen production, ORR and OER, two electron transfer

Posted Date: March 18th, 2022

DOI: https://doi.org/10.21203/rs.3.rs-1463731/v1

Abstract

Under the growing crisis of coronavirus disease 2019 pandemic, the global medical system is facing the predicament of an acute shortage of medical-grade oxygen (O_2, ≥ 99.5% purity). Herein, we manufactured an oxygen generation device relying on electrochemical technology. The performance of electrochemical oxygen generator (EOG) was remarkably improved to a practically applicable level, achieving long-term (>200 h), stable, and quick production (>1.5L/min) of high purity O_2 (99.9%) under high energy efficiency (496 L/kW·h), viasimultaneous optimizations for intrinsic electrochemical reaction mechanism, electrocatalysts, and external cell structure. The EOG also presents powerful competitiveness in user experience, which finds expression in high portability (4.7 kg), nearly instant O_2 production (<1 s), and a quiet working condition (<39 dB). The EOG shows great potential to substitute commercial pressure swing adsorption O_2 generation devices, which may significantly impact the traditional oxygen production industry.

Full Text

High-purity oxygen (O_2) is widely applied in a variety of industrial fields, including medical applications (hospitals, home care oxygen therapy), military defense (submarines, aircraft, and aerospace), metallurgical and glass processing (copper, steel and glass making, cutting, and welding), semiconductor manufacturing and food processing, etc[1,2]. In particular, due to the global outbreak of coronavirus disease 2019 (COVID-19) since December 2019, there was a sudden surge in demand for medical-grade oxygen (≥ 99.5% O_2 purity)[3] for the worldwide medical system[4]. At the current stage, the O_2 production industry generally adopts the physical air-separation strategy, which mainly relies on the technologies of cryogenic distillation and pressure swing adsorption (PSA) [2,5,6]. Although cryogenic distillation technology is the main way to produce high-purity oxygen for oxygen cylinders (99+% O_2 purity)[7], it requires bulky and complex production equipment, as well as substantial energy consumption, and strongly depends on developed transportations and safety capabilities to deliver the produced O_2. Therefore, this technology is unable to satisfy the requirements for in-situ O_2 production and constant O_2 supply, for responding to various unanticipated emergencies at hospitals under the pressure of COVID-19 (Fig. 1a). On the other hand, PSA technology is preferable for small- or medium-scale applications to meet the demand for in-situ O_2 production. It can separate O_2 from the air in an ambient environment, and gradually escalate its purity by multiple adsorption-desorption processes on the solid adsorbents (Fig. 1b). However, PSA technology only produces O_2 with limited purity of 93%±3[7-9]. To date, a technology that simultaneously achieves constant, portable, energy-saving, and in-situ production of high-purity O_2 has not yet been practically realized in the O_2 production industry.

Apart from the physical air-separation technology, chemical water electrolysis can generate high-purity O_2 by the oxidation of water. However, this process suffers from high energy consumption and is

accompanied by the production of explosive hydrogen as the by-product[10]. In 1964, Langer *et al.* first proposed an electrochemical strategy to generate O_2 by utilizing the electrolytic cell, where O_2 is selectively reduced from the air at the cathode by oxygen reduction reaction (ORR), and regenerated at the anode by oxygen evolution reaction (OER) via a four-electron transfer (4ET) pathway[11]. This electrochemical strategy was further developed by Goldstein *et al.* in 1972[12], who experimentally verified a more efficient route to produce O_2, by employing a two-electron transfer (2ET) pathway with the formation of HO_2^- as the intermediate species. Afterward, the viability of the above 2ET-route was supported by a study in 1981[13], which explicitly validated that the 2ET-electrochemical cell can greatly lower the energy consumption compared with those previous 4ET-ones. However, for those studies concerning electrochemical O_2 generation[10-15], restricted by the primitive cell structure and catalyst with inadequate activity and selectivity, the electrochemical cells presented relatively low current density, poor energy efficiency and weak stability, thus had not been further developed to an applicable device. Consequently, for decades, the electrochemical strategy has not received deserved attention followed by gradually faded out from the views. The O_2 production field has been invariably dominated by the physical air-separation strategy till now.

In the present work, we manufactured an oxygen generation device by means of electrochemical technology. The performance of the electrochemical oxygen generator (EOG) has been improved to a practically applicable level and finally achieved long-term, stable, and quick production of high purity O_2 under high energy efficiency via some targeted optimizations and elaborate designs. In comparison to previous studies, the optimized EOG cell presents notably surpassed performance in current density, electrode area, O_2 production rate, energy efficiency and O_2 purity, etc (Fig. 1c and Table S1). In particular, the energy efficiency of our EOG for the first time was improved to a comparable level (496 L/kW·h) to commercial PSA O_2 generation devices (152 L/kW·h~327 L/kW·h[7,9]), confirming the practical availability of the electrochemical technology in the oxygen production field. For the actual user experience aspects, the EOG also show strongly competitive power, reflecting in the generation of high O_2 purity reaching medical grade (99.9%), light and handy size to be easily carried and transported (4.7 kg), nearly instant O_2 generation for responding to sudden emergencies (<1 s), quiet working condition that is in favor of patients (<39 dB), and long stability for constantly providing O_2 (>200 h). As illustrated in Fig. 1d, the EOG remedies the drawbacks of inconvenient transportation and storage for oxygen cylinders, and insufficient O_2 purity for PSA devices. It can directly and quickly supply high purity O_2 to patients. Our work not only designed a portable, low-cost, energy-saving, and in-situ O_2 production device, but more importantly, developed the electrochemical strategy which was longtime neglected by the O_2 production field to a workable technology with industrial application significance.

The performance of the EOG cell is mainly affected by three polarization resistances, namely (1) electrochemical polarization: originates from the activation barriers of the cathodic ORR and anodic OER; (2) concentration polarization: brought by the rapid depletion of gas during the cathodic ORR under high current density, leading to retard the whole reaction rates; (3) ohmic polarization: derives from the ohmic

losses due to the ionic conduction in the electrolyte. Aiming to lower the above three polarization resistances, we conducted specific improvements in oxygen production mechanism, electrocatalysts, and cell structure, which effectively enhanced the performance of the EOG cell.

The electrochemical oxygen production is realized by two electrocatalytic reactions: the extraction of O_2 from the air through the cathodic ORR, and the generation of O_2 with the anodic OER. At an alkaline condition, the ORR and OER reactions can occur via two pathways, namely the 4ET and the 2ET pathways[16, 17]. The 4ET pathway adopts OH^- as the intermediate species, while the 2ET one applies HO_2^-. As shown in Fig. 2a, the 2ET pathway only consumes half of the electrons compared with the 4ET pathway in both ORR and OER processes. The previous reports have confirmed that the 2ET route is more energy-efficient compared with the 4ET-route [13,14.] Therefore, we adopted the 2ET-route as the oxygen production mechanism to decrease the intrinsic energy consumption in electrode reactions. Moreover, it is of great necessity to employ 2ET ORR and OER electrocatalysts with high activity and selectivity, so as to reduce the electrochemical polarization resistance from the electrode reactions. For the cathodic ORR process, we developed a general, low-cost, and facile strategy to access the large-scale synthesis of the 2ET-ORR electrocatalyst with high selectivity and activity. Commercial carbon black was chosen as raw material due to its low cost, excellent conductivity, high specific surface area, and porous structure for the high mass activity. According to recent studies, the 2ET selectivity was demonstrated to be strongly correlated with the species and content of oxygen-containing functional groups on oxidized carbon-based materials[18-21]. In our study, carbon black was oxidized by treating with ozone under the specified reaction times, resulting in a series of oxidized carbon black (O-C) nanoparticles with different oxygen surface contents (see materials and methods in Supporting Information). No morphological changes were observed for these O-C nanoparticles after ozone treatment (Fig. S1). The specific surface oxygen contents of O-C catalysts were characterized to be 0.4%, 1.4%, 11.3%, 18.8%, and 25.1% by X-ray photoelectron spectroscopy (XPS) analysis (Fig. S2), corresponding to 0, 4, 8, and 16 h reaction times of the ozone treatment, respectively. The ozone treatment introduced abundant oxygen-containing functional groups, including carboxyl ($-COO^-$), carbonyl (C=O), and hydroxyl (C-OH), on the surface of O-C catalysts, as deconvolved from carbon and oxygen 1s signals (Fig. S3). Apparently, the longer ozone-treatment times gave rise to a higher oxygen content until 25.1 % within 16 h (Fig. 2b). The XPS analysis of C 1s and O 1s spectra in Fig. 2c and S3 revealed that the carboxyl group $-COO^-$ is gradually enriched along with the ozone-treatment times. The above results are further reinforced by the Fourier-transform infrared (FTIR) spectra in Fig. S4, showing a positively proportional relationship between the ozone-treatment times and the content of $-COO^-$. XPS only detected C and O, and inductively coupled plasma optical emission spectrometry (ICP-OES) excluded other metal elements for the prepared catalysts, which verified the ozone treatment is a clean strategy without introducing impurities, consequently, getting rid of repeated purification steps. The ORR activity and selectivity for O-C catalysts with different oxygen contents were evaluated by a standard three-electrode rotating ring-disk electrode (RRDE) in a basic electrolyte (0.1 M KOH, pH~13), and the results are shown in Fig. S5. With the increase of oxygen contents on O-C surfaces, the activity and selectivity towards the 2ET pathway for ORR both increase first

and then start to decrease. Among them, O-C-18.8% exhibits the highest ORR and H_2O_2 generation current densities (Fig. S5a), as well as the best 2ET selectivity achieving 97.5% (Fig. S5b). However, O-C-25.1% shows both declined activity and selectivity despite containing the highest surface oxygen content. Brunner–Emmet–Teller (BET) measurements (Fig. S6) revealed that the introduction of abundant defects causes the collapse of the pore structure of the porous O-C catalysts and thus decreases the specific surface area. That is, the excessive surface oxygen coverage of O-C catalysts may deteriorate the performance of the 2ET activity for ORR due to the reduced reaction active area and weakened conductivity. The stability measurements of O-C-18.8% were conducted and the results are shown in Fig. S7 and Fig. S8. After 1000 cyclic voltammetry (CV) cycles between 0.4 and 0.9 V *vs*. RHE, the declines of the current density and the 2ET selectivity were less than 1% (Fig. S7). Moreover, the stability of the O-C-18.8% was demonstrated by the long-term test (~10 h) showing negligible changes in both activity and selectivity (Fig. S8). After optimization, the O-C-18.8% was selected as the cathode electrocatalyst for the EOG system and was synthesized with a simplified method on a large scale (defined as L-O-C (18.8%), Fig. S9). L-O-C (18.8%) was validated that contains nearly similar content and species of surface oxygen functional groups with O-C-18.8% ((Figs. 2d, 2e), indicating the viability of the large-scale synthesis method.

To compare the total energy consumption of whole electrochemical reactions regarding the 2ET and 4ET pathways, we will separately discuss ORR and OER processes by means of density functional theory (DFT) calculations. For the cathodic ORR electrocatalyst, the surface of O-C catalyst was simplified as a two-dimensional graphene monolayer with several oxygen-containing functional groups of –COOH, C=O, and –OH that were observed in the characterization experiments (Fig. 2c). The computational details can be seen in Supporting Information and all the configurations are displayed in Fig. S14-S16. Fig. 2f shows the relationship between the limiting potential (U_L) and the OH* binding energy (ΔG_{OH*}) for both 2ET- and 4ET-ORR pathways. For each type of O-C catalyst, whether it is on the left or right of the volcano map, the 2ET process always has a stronger thermodynamic driving force than the 4ET pathway due to the lower overpotential (η). In all the configurations, the carbon atoms adjacent to oxygen-containing functional groups are considered as active sites, and the 2ET-ORR activity varies by changing the local chemical environment of the oxygen-containing functional groups. Fig. 2f indicates that the O-C catalyst with $\Delta G_{OH*} > 1.3$ eV does not significantly contribute to the 2ET-ORR activity due to the η larger than 0.45 V. However, the O-C configurations with appropriate ΔG_{OH*} between 0.5 and 1.3 eV exhibit high 2ET-ORR activity due to the small η ranging from 0.06 to 0.41 V. Among these configurations, we find that the carbon site with two –COOH groups on zigzag carbon edges (Fig. 2f) is most active, yielding a η of only 0.06 V. This result implies that the excellent activity of the prepared O-C catalysts towards 2ET-ORR might be ascribed to the high content ratio of –COOH in oxygen-containing functional groups (Fig. 2b). It is also important to note that most of the computed η values on O-C following the 2ET-ORR mechanism are even lower than that (0.45 V) on the traditional Pt catalyst through the 4ET-ORR process[22]. The above calculated results provide a compact explanation for both the observed high activity and selectivity of O-C toward the 2ET-ORR. For the anodic OER process, FeNi-Layered Double Hydroxide (LDH) was used as the electrocatalyst, which shows superior performance to commercial IrO_2 and RuO_2 in both activity and

stability (Fig. S10). As the reverse reaction of ORR, OER occurs via whether the 4ET or 2ET pathway is determined by the intermediate species OH^- or HO_2^- generated during ORR. Previous theoretical studies[23-25] on FeNi-LDHs suggest that the 2ET-OER is easier to take place than the 4ET-OER (see Supporting Information for detailed discussion). The above theories demonstrated that ORR and OER both obtain lower overpotentials via the 2ET pathway than the 4ET pathway, indicating less energy consumption by adopting the 2ET pathway.

The cathodic ORR is essentially a three-phase interfacial reaction involving catalytic active sites, electrolytes, and gaseous reactants. Under a large current density, the activity of ORR is severely restricted by the insufficient mass transfer of the gaseous reactants towards ORR-catalyst surfaces. In view of this, we introduced a gas diffusion electrode (GDE) into the EOG cell to promote the ORR rate (Figs. 3a, 3b, and S11). GDE consists of a current collector, a highly hydrophobic microporous gas diffusion layer (GDL), and a catalyst layer (CL). The current collector bears mechanical strength and conductivity, which supports the structure and electron transmission during the electrochemical reactions. The GDL contains numerous microporous flow channels which are in favor of gaseous reactants transport towards the CL, and meanwhile, preventing itself from being wetted by the electrolyte due to the high hydrophobicity. Such designs endow EOG cell with continuous, rapid, and stable gas-feeding for ORR, and accordingly, reduces its concentration polarization resistance.

In an actual electrochemical reaction system, the inner resistance of the electrolytic cell brought by the ohmic polarization will induce apparent potential drops, which may cause side reactions and significantly lower energy efficiency. Therefore, an imidazole-functionalized alkaline anion exchange membrane (AEM) was synthesized[26] and placed between cathodic GDE and anode. Such a compact sandwich structure makes the electrodes achieving “zero-gap”, lowering the ohmic losses to the greatest extent[27, 28], and in particular, improving the stability of the cell system by lowering heat generation. Besides, the AEM merely allows anions to pass through but entirely blocks air, which plays an immensely critical role in obtaining O_2 with high purity.

Fig. 3a illustrates the exploded schematic of the EOG cell. Behind the cathodic GDE and anode sides, seal gaskets made of fluorinated ethylene propylene, serpentine flow plates made of stainless steel with nickel plating, copper conductive plates, and end plates made of epoxy resin were arranged in order, and all the elements were firmly secured by bolts. Figs. 3c exhibits the working mechanism of the EOG cell: at the cathode, the upper vent is fed with air where O_2 is converted into an ionic state of HO_2^- by ORR, and the O_2-depleted air is expelled from the lower vent. At the anode, the intermediate species HO_2^- migrates to here through AEM driven by potential difference, and is oxidized to generate pure O_2. Finally, the generated O_2 is released along with the flowing anodic electrolyte. After passing through the water vapor filter, the produced O_2 can be directly collected, and the purity of O_2 was analyzed to 99.9% (Fig. S12 and Table S3). The whole electrochemical reactions take place in a mild reaction condition without producing any contaminations. The performance of the unit EOG cell (16 cm^2 working area) with the loading of Pt/C and a series of O-C catalysts were investigated. The corresponding current-voltage (*I-V*) curves and the

Faradaic efficiency are shown in Fig. 3d and 3e. Among O-C catalysts, O-C-18.8% presents the lowest cell voltage (0.87 V under 200 mA cm^{-2}), as well as the optimal 2ET selectivity of ORR (over 90% Faradaic efficiency of 2ET pathway). Meanwhile, L-O-C (18.8%) displays similarly excellent performance and selectivity with O-C-18.8%, confirming the reliability of the large-scale synthesis. No H_2 byproduct was detected from the cathode side under such high current density, indicating the exclusive selectivity for ORR. The numbers of transferred electrons over O-C-18.8% and L-O-C (18.8%) were calculated to be ~2.1 (equation A in Supporting Information), which demonstrated a typical 2ET pathway for ORR. To validate the scalability of the electrochemical cell, the polar plates with a 100 cm^2 working area were used for performance evaluation in a one-unit modular cell. As illustrated in Fig. 3d and 3f, the L-O-C (18.8%) in the amplified cell presents no degradation of performance compared with that in the small-scale cell (16 cm^2 working area). In Fig. 3g and S13, L-O-C (18.8%) exhibits 147 mL/min of O_2 production rate and 511 L/kW·h of energy efficiency (defined by the ratio of O_2 production rate to power) under the same cell current of 20 A. While for Pt/C, despite it shows a slightly lower cell voltage of ORR (Fig. 3f and 3g), its O_2 production rate and energy efficiency are only approximate to a half level of the L-O-C (18.8%) (76 mL/min and 270 L/kW·h). In conclusion, L-O-C (18.8%) not only has a significantly cheaper cost of the raw material than Pt/C, but also greatly lowers the energy consumption through the 2ET pathway of ORR and OER.

Several polar plates with 100 cm^2 working area are piled in series to assemble into a cell stack comprising 9-unit cells, which aims to reach a high O_2 production rate and minimize the volume and weight (Fig. 4). The bipolar plates are elaborately structured to guarantee the continuous and smooth operation of the cell stack under a high current density. As shown in the schematic (Fig. 4a), the distribution area is added to uniformly allocate the fluid and air flows of the main channels towards the bipolar plate of each unit cell, creating a consistent working environment among each unit cell. The bipolar plate is configured with multiple sets of parallel serpentine flow channels, which ensures the uniform distribution of gas and liquid medium and the proportion of the reactive area. In addition, the multiple sets of serpentine flow fields can also minimize the number of turns and the length of flow channels, dramatically reducing the pressure loss and ensuring adequate mass transfer. Hence, the cell stack can realize stable operation under a high current density to guarantee the production rate of O_2. By controlling the applied voltage, the O_2 production rate of the as-assembled EOG cell stack can be regulated in the range from 0.35 to 2.66 L/min (Fig. 4b). For the stability measurements, the EOG device exhibits a constant O_2 production rate around 1.5 L/min and a steady current with less than 1% decay within 200 h (Fig. 4c), exhibiting an excellent stability performance.

Table 1. Comparative data of EOG device and PSA device.

O_2 Generation Devices (under the same O_2 production rate: 1.5 L/min)	Energy efficiency	O_2 Purity	Noise level	weight	Start-up time
EOG	496 L/kW·h	99.9%	38.5 dB	4.7 kg	<1 s
PSA	234~327 L/kW·h[a] 152~321 L/kW·h[b] 250 L/kW·h[c]	93.6%	93.6 dB	15.6 kg	≈20 s

a, b Data for stationary PSA devices is from the ref 7 and 9, respectively. The energy efficiency is varied depending on the model.

c Data is from the product information of the purchased PSA device in the present study. The detailed product information is in Supporting Information.

The main performance index of the EOG device designed in this study is compared with a commercial PSA device in energy efficiency, O_2 purity, noise level, weight, and start-up time, and the results are shown in Table 1. The working conditions of the EOG and PSA devices are recorded in Figs. 4d, 4e, and Video S1. Results indicate that the energy efficiency of the EOG device attains a comparable level for various commercial PSA devices under the same O_2 generation rate (1.5 L/min). The purity of O_2 generated by the EOG device is up to 99.9%, while that of PSA device is measured to be only 93.6%. In essence, EOG is a device based on the electrochemical technology, where nearly pure O_2 can be easily obtained via electrocatalytic reactions. That is distinguished from the PSA technology, where O_2 purity is limited due to the incomplete adsorption-desorption processes. Medically, less noise level of O_2 generation devices is of great importance to hospitals and patients. As shown in Table 1, the noise generated by the air compressor of the PSA device is up to 93.6 dB (equivalent to the start-up sound of an automobile engine), which may cause negative side effects for patients. In contrast, the noise level of the EOG device is only 38.5 dB (equivalent to the working sound of a laptop), which is more suitable for applying at home or wards. In terms of portability, the PSA device weighs about 15.6 kg, where the irreplaceable air compressor and adsorbing canister account for the weight in a large proportion. Relatively, the EOG device weighs as light as 4.7 kg with the generation of equivalent O_2 of the PSA device, realizing the portable in-situ O_2 generation. Finally, the two devices will be compared regarding the start-up time. Generally, obtaining concentrated O_2 by PSA device costs around 20 s from its startup due to multiple cycles of adsorption and desorption processes. It is hard to address the emergency need of patients in severe conditions for medical oxygen. However, the EOG device generates medical oxygen nearly instantly which can well satisfy the urgent needs in a variety of conditions. The items in Table 1 are plotted into a five-star chart to compare these two O_2 generation devices visually. As can be seen in Fig. 4f, the EOG device shows apparently superior user experiences (O_2 purity, energy efficiency, start-up time,

weight, and noise level) to those of commercial PSA devices, which has great market potential in the O_2 production field.

Conclusions

In summary, our work designed an EOG and improved its performance to an applicable level. Such remarkable enhancement of the performance originates from the targeted optimizations for intrinsic oxygen production mechanism, electrocatalysts, and external cell structure. Our EOG is powerfully competitive compared with the commercial PSA devices, which is reflected in the comparable energy efficiency, higher O_2 purity, lighter device weight, lower noise level, and quicker start-up time. Under the severe pressure of COVID-19, our EOG is expected to be ideal medical-oxygen supply equipment for patients in a variety of emergency conditions, and fill the great shortage of O_2 generation devices in the worldwide market.

Declarations

SUPPLEMENTARY INFORMATION

The Supplementary Information includes Supplementary Methods, Supplementary Figures S1-S16, Supplementary Tables S1-S3 and Supplementary Video S1.

AUTHOR CONTRIBUTIONS

Author Contributions: Y. Z. and C. Z. carried out the sample synthesis, characterization, and electrochemical measurements. K. X., F. W. and S. L. co-contributed to the theoretical studies. Y. Z. and Y. W. co-wrote the paper. Q. X., J. H., H. D. and J. Z. performed the X-ray photoelectron spectroscopy experiments. F. Z., P. L., Y. T. and D. L. helped with the modification of the paper. All authors participated in the discussion of the results, commented on the implications, and fully approved the content of the manuscript.

† These authors contributed equally to this work.

ACKNOWLEDGMENTS

This work was supported by National Key R&D Program of China 2017YFA (0208300, 0700104), the DNL Cooperation Fund, CAS (DNL201918), the Fundamental Research Funds for the Central Universities (WK2060120004, WK2060000021, WK2060000025 and KY2060000180)the National Natural Science Foundation of Fujian Province, China (2020J02025), and National Natural Science Foundation of China (21973013). This work was partially carried out at the USTC Center for Micro and Nanoscale Research and Fabrication. Thank the funding support from CAS Fujian Institute of Innovation, and the “Chuying Program” for the Top Young Talents of Fujian Province. We acknowledge the Experimental Center of Engineering and Material Science in the University of Science and Technology of China. We thank the

photoemission endstations BL1W1B in Beijing Synchrotron Radiation Facility (BSRF), BL14W1 in Shanghai Synchrotron Radiation Facility (SSRF), BL10B and BL11U in National Synchrotron Radiation Laboratory (NSRL) for the help in characterizations.

DECLARATION OF INTERESTS

The authors declare no competing interests.

References

1. Tsuru, T., & Hwang, S.-T. Production of high-purity oxygen by continuous membrane column combined with PSA oxygen generator. *Ind. Eng. Chem. Res.* **33**, 311-316 (1994).

2. Hejazi, S. A. H. *et al.* Dynamic column breakthrough and process studies of high-purity oxygen production using silver-exchanged titanosilicates. *Ind. Eng. Chem. Res.* **55**, 5993-6005 (2016).

3. Oxygen (Oxygenium). The International Pharmacopoeia (ed. 10, 2020), pp. 1-5.

4. Usher, A. D. Medical oxygen crisis: a belated COVID-19 response. *The Lancet* **397**, 868-869 (2021).

5. Hayashi, S., Kawai, & M., Kaneko, T. Dynamics of high purity oxygen PSA. *Gas. Sep.Purif.* **10**, 19-23 (1996).

6. Santos, J. C. *et al.* High-purity oxygen production by pressure swing adsorption. *Ind. Eng. Chem. Res.* **46**, 591 (2007).

7. Technical specifications for oxygen concentrators, WHO medical device technical series. World Health Organization (2015).

8. Technical specifications for Pressure Swing Adsorption (PSA) Oxygen Plants: Interim guidance. World Health Organization (2020).

9. Ackley, M. W. Medical oxygen concentrators: a review of progress in air separation technology. *Adsorption* **25**,1437-1474 (2019).

10. Giddey, S., Ciacchi, F. T., Badwal, & S. P. S High purity oxygen production with a polymer electrolyte membrane electrolyser. *J. Membrane Sci.* **346**, 227-232 (2010).

11. Langer S. H., & Haldeman, R. G. Electrolytic Separation and Purification of Oxygen from a Gas Mixture. *J. Phys. Chem.* **68**, 962-963 (1964).

12. Goldstein J. R., & Tseung, A. C. C. Kinetics of Oxygen Reduction on Graphite|Cobalt-Iron Oxide Electrodes with Coupled Heterogeneous Chemical Decomposition of H_2O_2. *J. Phys. Chem.* **7**, 3646-4656 (1972).

13. Tseung, A. C. C., & Jasem, S. M. An integrated electrochemical-chemical method for the extraction of O_2 from air. *J. Appl. Electrochem.* **11**, 209-215 (1981).

14. Yuko, F. *et al*. An electrochemical oxygen separator using an ion-exchange membrane as the electrolyte. *J. Appl. Electrochem.* **16**, 935-940 (1986).

15. Brillas, E., Maestro, A., & Moratalla, M. Electrochemical extraction of oxygen from air via hydroperoxide ion. *J. Appl. Electrochem.* **27**, 83-92 (1997).

16. Shao, M. *et al.* Recent advances in electrocatalysts for oxygen reduction reaction. *Chem. Rev.* **116**, 3594-3657 (2016).

17. Kulkarni, A. *et al.* Understanding catalytic activity trends in the oxygen reduction reaction. *Chem. Rev.* **118**, 2302-2312 (2018).

18. Wu, K.-H. *et al.* Highly selective hydrogen peroxide electrosynthesis on carbon: in situ interface engineering with surfactants. *Chem* **6**, 1443-1458 (2020).

19. Lu, Z. *et al.* High-efficiency oxygen reduction to hydrogen peroxide catalysed by oxidized carbon materials. *Nat. Catal.* **1**, 156-162 (2018).

20. Tan, X., Tahini, H. A. & Smith, S. C. Understanding the high activity of mildly reduced graphene oxide electrocatalysts in oxygen reduction to hydrogen peroxide. *Mater. Horiz.* **6**, 1409-1415 (2019).

21. Melchionna, M., Fornasiero, P. & Prato, M. The rise of hydrogen peroxide as the main product by metal-free catalysis in oxygen reductions. *Adv. Mater.* **31**, 1802920 (2019).

22. Nørskov, J. K. *et al*. Origin of the Overpotential for Oxygen Reduction at a Fuel-Cell Cathode. *J. Phys. Chem. B* **108**, 17886-17892 (2004).

23. Wang, X. *et al.* Ta-doping triggered electronic structural engineering and strain effect in NiFe LDH for enhanced water oxidation. *Chem. Eng. J.* **403**, 126297 (2021).

24. Fan, K. *et al.* Nickel–vanadium monolayer double hydroxide for efficient electrochemical water oxidation. *Nat. Commun.* **7**, 11981 (2016).

25. Xiao, H., Shin, H. & Goddard, W. A. Synergy between Fe and Ni in the optimal performance of (Ni,Fe)OOH catalysts for the oxygen evolution reaction. *PNAS* **115**, 5872-5877 (2018).

26. Liu, Z. *et al.* CO_2 electrolysis to CO and O_2 at high selectivity, stability and efficiency using sustainion membranes. *J. Electrochem. Soc.* **165**, J3371-J3377 (2018).

27. Z. Yin *et al*., An alkaline polymer electrolyte CO_2 electrolyzer operated with pure water. *Energy Environ. Sci.* **12**, 2455-2462 (2019).

28. Zhao, C. *et al.* In Situ Topotactic Transformation of an Interstitial Alloy for CO Electroreduction. *Adv. Mater.* **32**, 2002382 (2020).

Figures

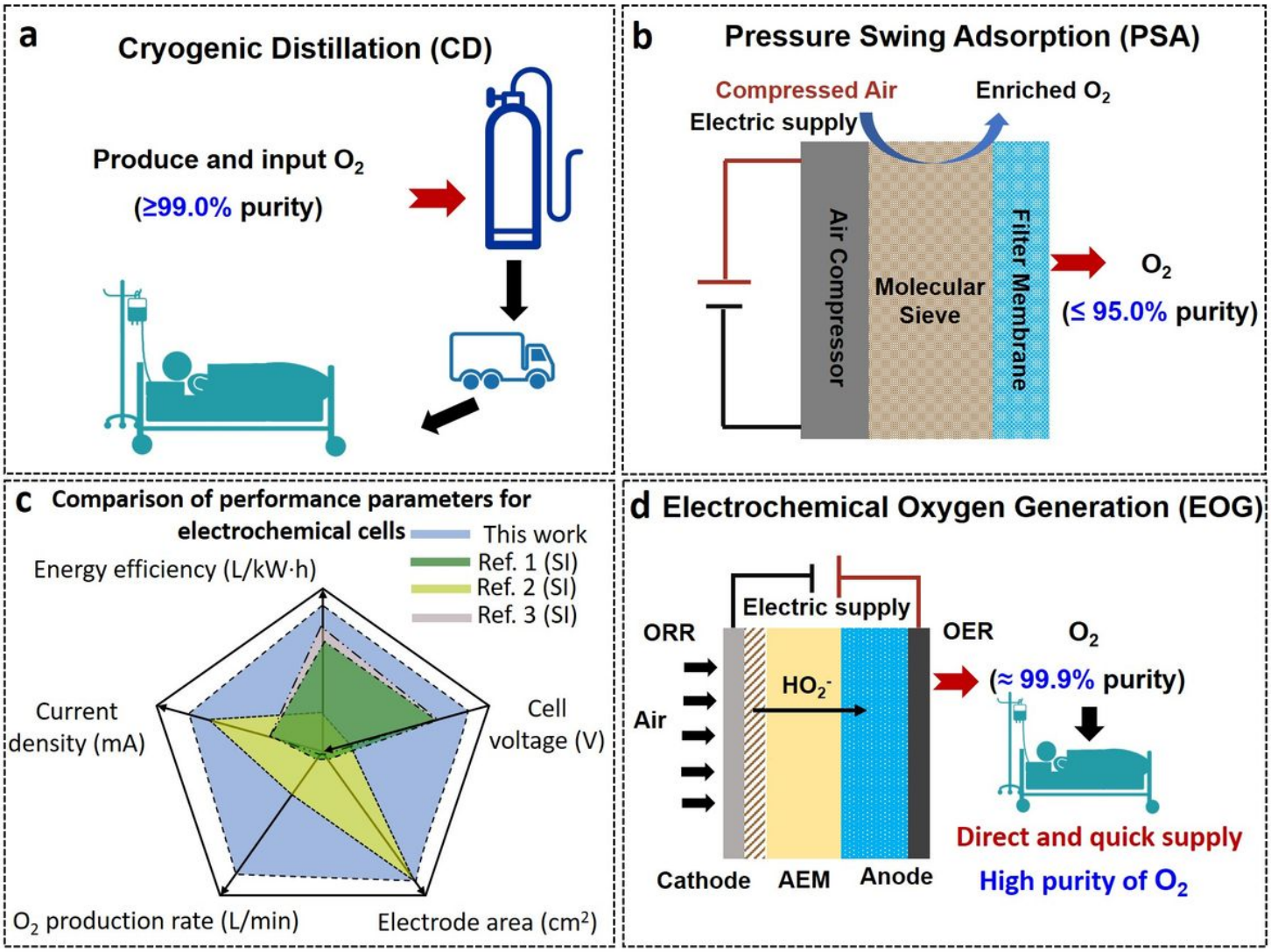

Figure 1

Schematic illustration of the comparison for three types of O_2 generation technologies (a, b, d), and performance parameters for electrochemical cells for this work and other research (c). a CD technology produces O_2 for oxygen cylinder with a high purity over 99%, however, cannot satisfy the supply due to the transport and storage issues under urgent and massive demands. **b**, PSA technology can realize the in-situ production of O_2, but the purity of the produced O_2 is not up to the standard of medical-grade oxygen. **c**, the comparison of performance parameters for electrochemical cells for this work and other research. **d**, EOG technology combines the advantages of the high purity of CD and the in-situ production of PSA, which can directly produce O_2 with the purity of 99.9% and then quickly supply to demanders.

Figure 2

Characterization analysis of 2ET-ORR electrocatalysts. a, ORR-OER mechanisms via 2ET or 4ET pathway; **b**, The surface oxygen contents of O-C catalysts after specific ozone-treatment times; **c**, XPS spectra of O 1s regions of O-C with different surface oxygen contents; NEXAFS spectra of C K-edge **d** and O K-edge **e** for the L-O-C (18.8%) and the O-C-18.8%；**f**, DFT calculated 2ET- (red) and 4ET- (blue) ORR volcano plots in which the limiting potential (U_L) is plotted as a function of ΔG_{OH}. The plots based on the RHE scale with the equilibrium potentials for both 2ET- and 4ET-ORR are displayed as dashed red and blue lines, respectively. Note that the 4ET-ORR activity of Pt(111) indicated by a yellow star is from ref 22. Carbon, oxygen, and hydrogen atoms are shown by grey, read, and white colors, respectively.

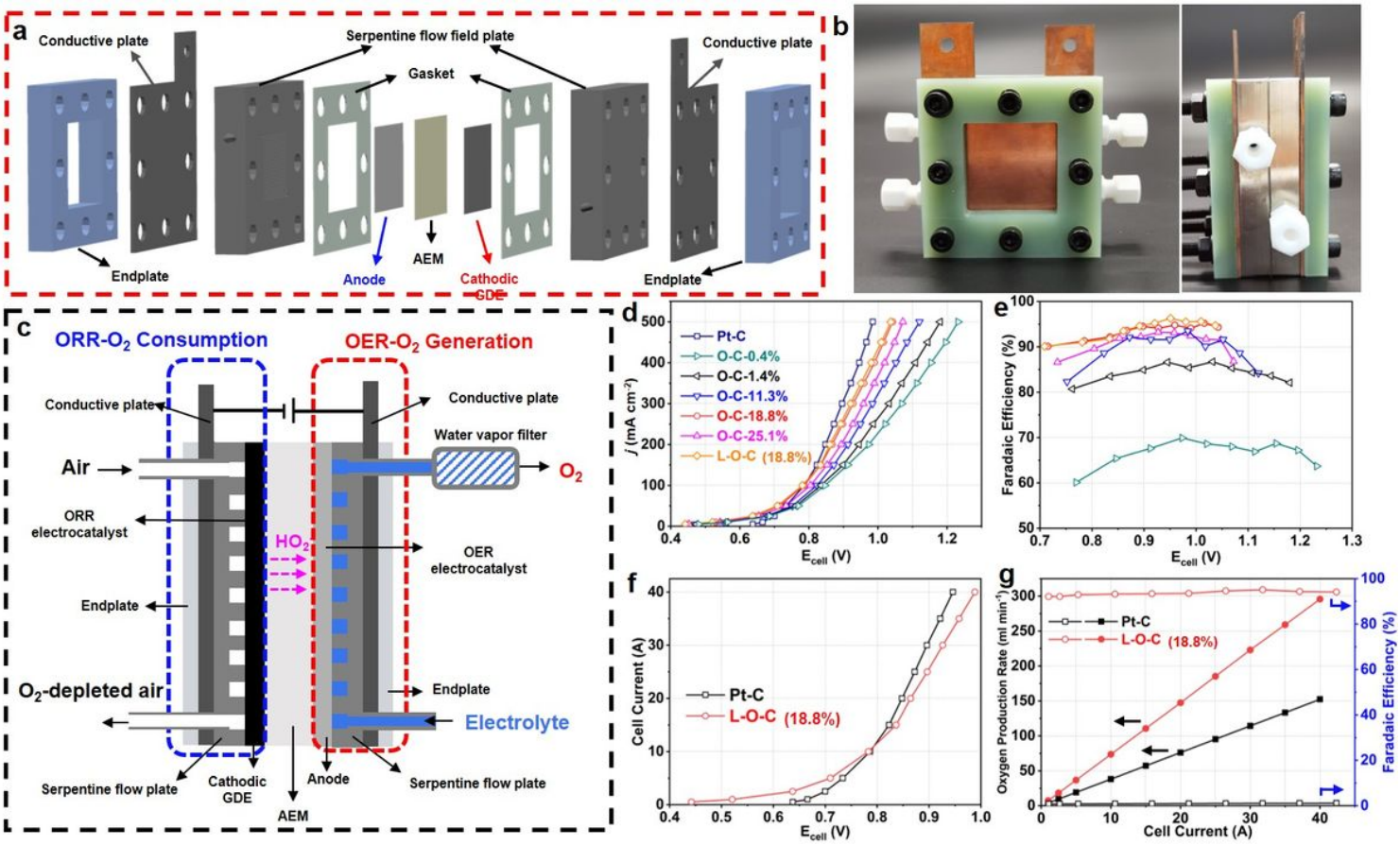

Figure 3

Performance characterization of 2ET-ORR electrocatalysts on the unit cell of EOG. a, The exploded schematic, **b**, digital photos and **c**, schematic diagram of the working mechanism for the unit cell of EOG. **d**, *I-V* curves and **e**, Faradic efficiency of Pt/C and a series of O-C catalysts for the unit cell of EOG with a 16 cm^2 working area. **f**, *I-V*curves, **g**, Faradic efficiency and O_2 production rate of Pt-C and L-O-C (18.8%) for the unit cell of EOG with a 100 cm^2working area.

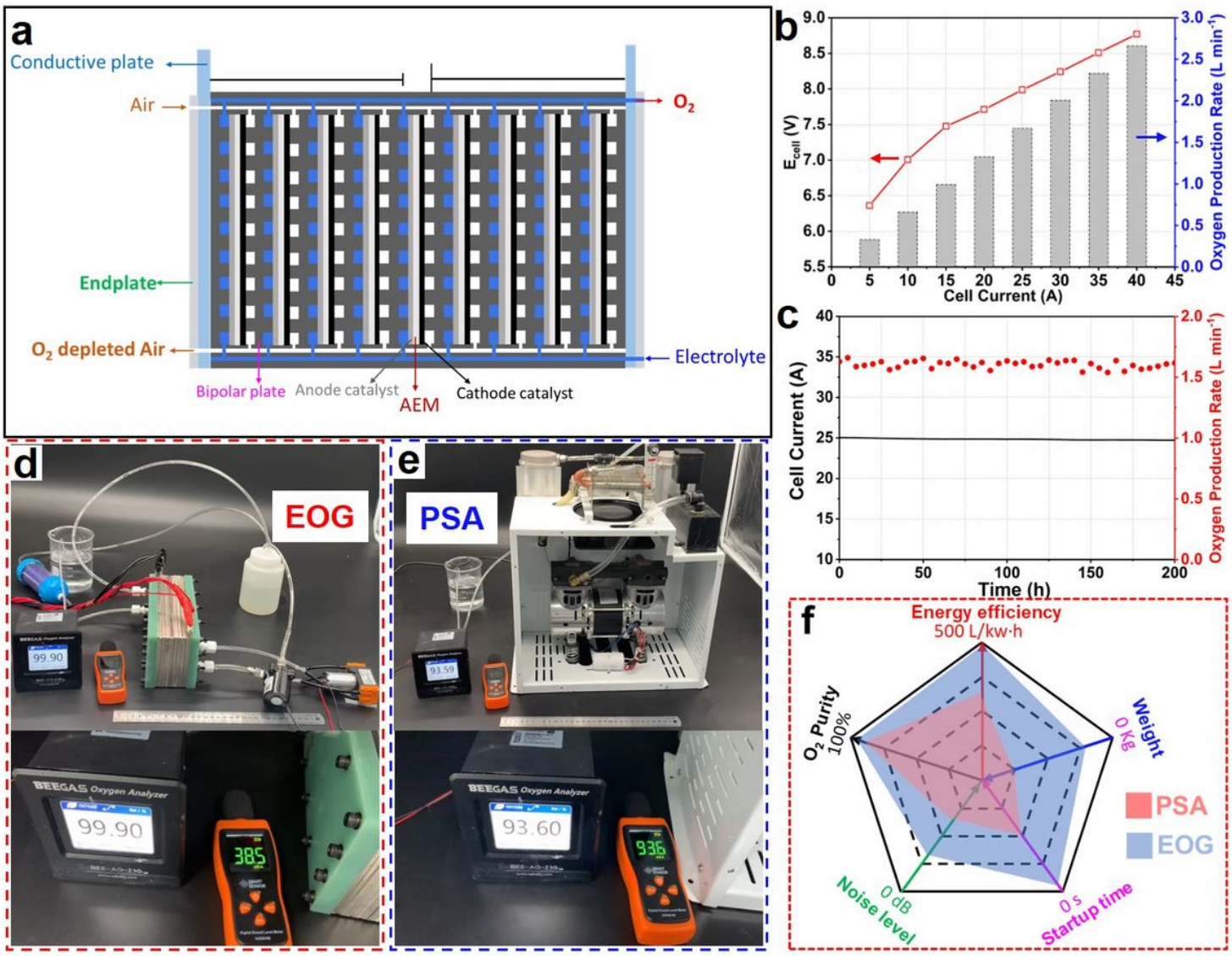

Figure 4

Performance characterization of the EOG cell stack. a, The structure schematic of the EOG cell stack comprising 9-unit cells. **b**, *I-V* curves and O_2 production rates of the EOG cell stack with a 100 cm^2 working area. **c**, Stability test of the EOG cell stack. The digital photos showing the comparison of **d** EOG and **e** PSA devices for O_2 purity (value on black apparatus) and noise (value on orange apparatus). **f**, Five-star chart showing the comparison of the user experience for EOG and PSA devices.

Supplementary Files

This is a list of supplementary files associated with this preprint. Click to download.

- SupportingInformation.docx
- SI.mp4